

# Interface-Charge Induced Giant Electrocaloric Effect in Lead Free Ferroelectric Thin-Film Bilayers

Sagar E. Shirsath,<sup>†</sup> Claudio Cazorla,<sup>†</sup> Teng Lu,<sup>‡</sup> Le Zhang,<sup>†</sup> Yee Yan Tay,<sup>§</sup> Xiaojie Lou,<sup>||</sup> Yun Liu,<sup>‡</sup> Sean Li,<sup>†</sup> and Danyang Wang<sup>\*,†</sup>

<sup>†</sup>School of Materials Science and Engineering, University of New South Wales, Sydney, New South Wales 2052, Australia

<sup>‡</sup>Research School of Chemistry, The Australian National University, Canberra, Australian Capital Territory 2601, Australia

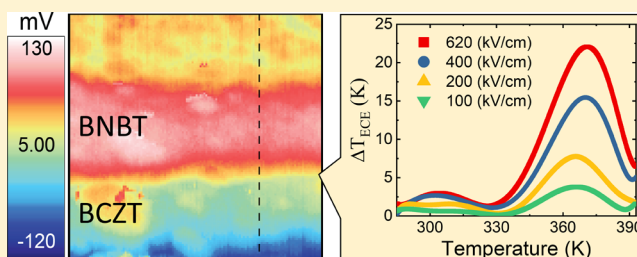
<sup>§</sup>Facility for Analysis, Characterization, Testing and Simulation and School of Materials Science and Engineering, Nanyang Technological University, 50 Nanyang Avenue, 639798 Singapore

<sup>||</sup>Multi-disciplinary Materials Research Centre, Frontier Institute of Science and Technology, and State Key Laboratory for Mechanical Behavior of Materials, Xi'an Jiaotong University, Xi'an 710049, China

## Supporting Information

**ABSTRACT:** Conventional refrigeration methods based on compression–expansion cycles of greenhouse gases are environmentally threatening and cannot be miniaturized. Electrocaloric effects driven by electric fields are especially well suited for implementation of built-in cooling in portable electronic devices. However, most known electrocaloric materials present poor cooling performances near room temperature, contain toxic substances, and require high electric fields. Here, we show that lead-free ferroelectric thin-film bilayers composed of  $(\text{Bi}_{0.5}\text{Na}_{0.5})\text{TiO}_3$ – $\text{BaTiO}_3$  (BNBT) and  $\text{Ba}(\text{Zr}_{0.2}\text{Ti}_{0.8})\text{O}_3$ – $(\text{Ba}_{0.7}\text{Ca}_{0.3})\text{TiO}_3$  (BCZT) display unprecedentedly large electrocaloric effects of  $\sim 23$  K near room temperature under moderate electric bias. The giant electrocaloric effect observed in BNBT/BCZT bilayers, which largely surpasses the sum of the individual caloric responses measured in BNBT and BCZT, is originated from the presence of compositional bound charges at their interface. Our discovery of interface charge-induced giant electrocaloric effects indicates that multilayered oxide heterostructures hold tremendous promise for developing highly efficient and scalable solid-state cooling applications.

**KEYWORDS:** Lead-free ferroelectrics, electrocaloric effect, thin film bilayer, first-principles calculations



Current vapor-compression cooling technologies employ harmful gases and cannot be scaled down to microchip dimensions. Other downsides of these technologies include undesired noise and slow start-up. The ever increasing world's population demands more comfortable living conditions that increasingly rely more on electronic platforms and portable devices; thus, it is crucial that we prioritize the development of alternative and bettered refrigeration technologies. Caloric materials react thermally to external stimuli (magnetic, mechanic, or electric) as a result of field-induced phase transformations that involve large changes in entropy. The compactness and fast response of caloric materials raise high hopes to surpass the performance, environmental compliance, and portability of current refrigeration technologies. A major breakthrough occurred in the late 1990s with the discovery of giant magnetocaloric effects;<sup>1</sup> nevertheless, most of the magnetocaloric materials are based on scarce rare-earth elements and require a high magnetic field. On the other hand, mechanocaloric effects are attracting much attention due to their large latent heat and huge adiabatic temperature changes;<sup>2–4</sup> the practical implementation of mechanocaloric

effects, however, becomes seriously compromised while moving down toward microchip dimensions.

In the context of microelectronic cooling, electrocaloric materials emerge as particularly promising owing to their high-energy density, natural integration in circuitry,<sup>5–8</sup> and the possibility to implement charge-recovery strategies for increasing their efficiency.<sup>9</sup> The prototype electrocaloric materials are ferroelectrics, which display a spontaneous electric polarization that can be broadly modulated with an external electric field at temperatures close to their paraelectric transition point. Yet, unfortunately, the largest electrocaloric effects (ECE) observed to date occur at nonambient conditions,<sup>10</sup> require large electric field (that end up giving rise to large leakage current and dielectric loss problems),<sup>11,12</sup> and/or involve materials that contain toxic substances (e.g., lead).

**Received:** November 15, 2019

**Revised:** December 24, 2019

**Published:** December 26, 2019

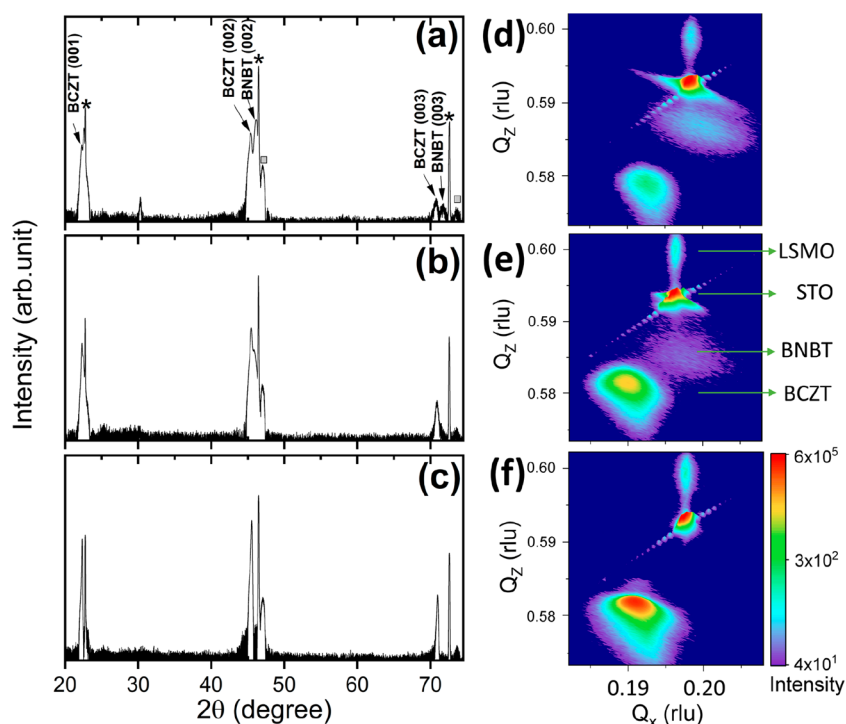


**Figure 1.** Left column: XRD patterns of (a) BNBT<sub>300</sub>/BCZT<sub>100</sub>, (b) BNBT<sub>200</sub>/BCZT<sub>200</sub>, and (c) BNBT<sub>40</sub>/BCZT<sub>360</sub>, where \* and □ represent STO substrate and LSMO (001) peaks, respectively. Right column: RSM plots of (d) BNBT<sub>300</sub>/BCZT<sub>100</sub>, (e) BNBT<sub>200</sub>/BCZT<sub>200</sub>, and (f) BNBT<sub>40</sub>/BCZT<sub>360</sub>.

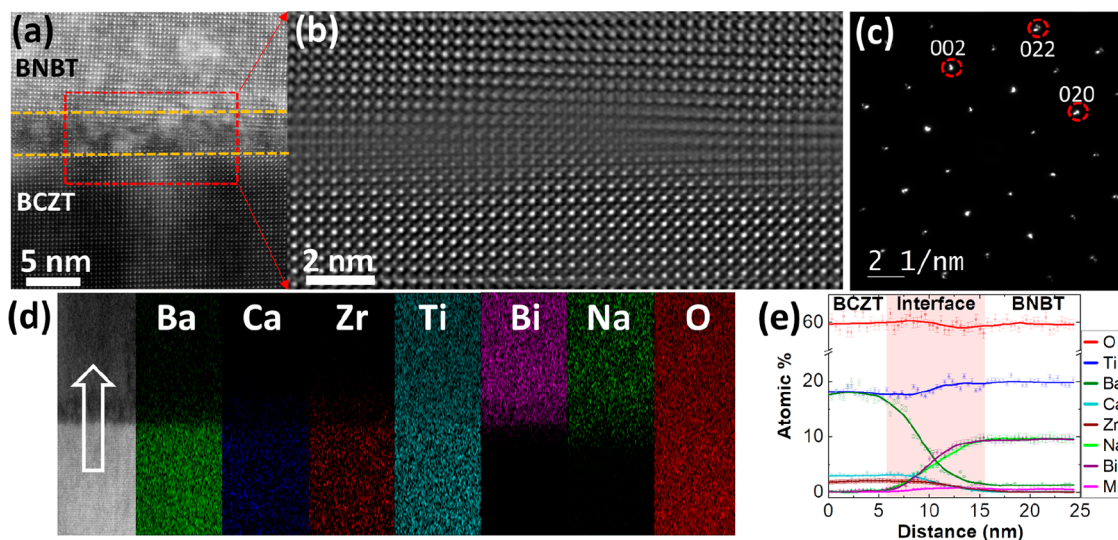


**Figure 2.** TEM and EDAX measurements of BNBT<sub>200</sub>/BCZT<sub>200</sub> samples. (a) Cross-sectional high-resolution HAADF-STEM image across the interface of the BNBT and BCZT layer region between the dotted-yellow lines indicates the interface of the BNBT and BCZT layer. (b) FFT analysis of the red-marked area of interface to visualize the intermixing of elements. (c) SAED pattern along [100] zone axis. (d) Color- and (e) line-mapping of elements by EDAX; arrow in TEM panel d indicates the direction of line mapping from BCZT to BNBT layer through their interface.

Here, we propose a new materials design strategy to overcome the common problems encountered in electrocaloric compounds, thus advancing the field of solid-state cooling. In particular, we investigated with experimental and theoretical techniques ECE in epitaxial bilayers consisting of 0.94-(Bi<sub>0.5</sub>Na<sub>0.5</sub>)TiO<sub>3</sub>-0.06BaTiO<sub>3</sub> (BNBT) and 0.5(Ba<sub>0.7</sub>Ca<sub>0.3</sub>)-TiO<sub>3</sub>-0.5Ba(Zr<sub>0.2</sub>Ti<sub>0.8</sub>)O<sub>3</sub> (BCZT) thin films grown on STO (001) single crystal substrates. First, by considering lead-free ferroelectric relaxors instead of customary ferroelectrics we

expand the temperature window in which the ferro-to-paraelectric phase transition occurs,<sup>13</sup> hence enlarging the operational range of ECE. And second, by considering multilayer oxide heterostructures we can explore the influence of interface effects and electrostatic coupling<sup>14,15</sup> on the global electrocaloric response of the material. Actually, we measure indirectly a giant ECE of ~23 K in a BNBT<sub>200</sub>/BCZT<sub>200</sub> bilayer (subscripts refer to the thin-film thickness in nm) near room temperature and under moderate electric fields ( $E \sim 600$

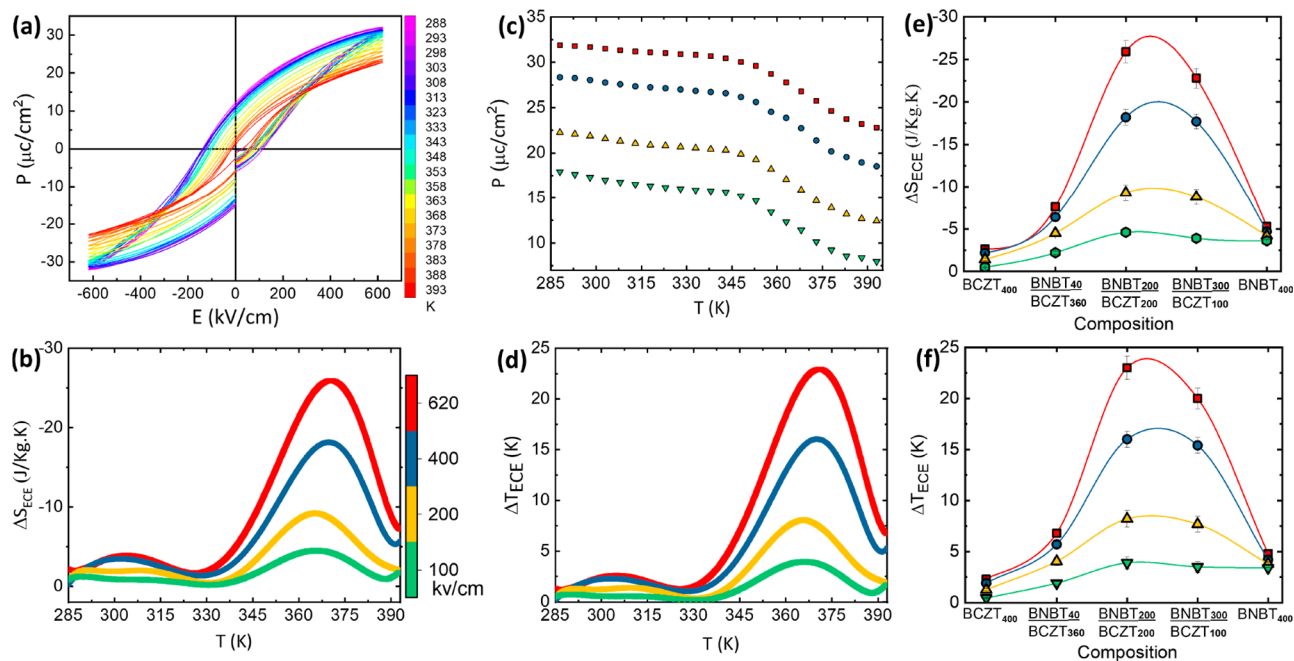


**Figure 3.** EC results of BNBT<sub>200</sub>/BCZT<sub>200</sub> bilayer sample. (a)  $P$ - $E$  loops measured as a function of temperature under maximum electric field,  $E$ , of 620 kV/cm, measurements were carried out at a fixed frequency of 1 kHz. (b) Plots of isothermal entropy,  $\Delta S_{ECE}$ , change versus temperature. (c) Variation of polarization as a function of temperature under four different electric fields. (d) Plots of adiabatic temperature,  $\Delta T_{ECE}$ , change versus temperature measured under four different electric field, comparative results of (e)  $\Delta S_{ECE}$  and (f)  $\Delta T_{ECE}$  for all the samples.

kV/cm). It is shown that the disclosed giant ECE in bilayer is significantly larger than the ECE measured in BNBT and BCZT monolayers, which is caused by the presence of compositional bound charges at the bilayer interface.

**Results. Thin Films and Interface Charge Characterization.** XRD patterns of the BNBT<sub>300</sub>/BCZT<sub>100</sub>, BNBT<sub>200</sub>/BCZT<sub>200</sub> and BNBT<sub>40</sub>/BCZT<sub>360</sub> bilayer samples are shown in Figure 1. Only (001) reflections are detected and no impurity or secondary phases are observed. It is clearly observed that the angular positions of peaks related to BCZT thin films almost do not change as the layer thickness varies. However, the BNBT peaks shift to higher angles when the thickness of the BNBT layer increases and the thickness of the underneath BCZT layer decreases. This is related to the difference in lattice parameters between the BNBT and BCZT layers. The out-of-plane (OOP) lattice constant,  $c$ , in the BCZT thin film increases slightly from 4.012 to 4.020 Å ( $\pm 0.002$  Å) as its thickness decreases. On the other hand, the OOP lattice parameter in the BNBT thin film increases considerably from 3.945 to 3.971 Å ( $\pm 0.002$  Å) as its thickness decreases from 400 to 40 nm.

Reciprocal space mapping (RSM) around the asymmetric (103) plane was performed to further understand the strain mechanism in BNBT/BCZT bilayers. The BNBT and BCZT peaks broaden both horizontally and vertically, confirming their mosaicity and lattice parameter variations. Furthermore, the spots corresponding to BNBT and BCZT reflections are not lined-up along the STO cubic reflection line, thus indicating that strains in these films are fully relaxed due to the significant lattice mismatch between the layers and the substrate. However, a lower strain level is still possible in the vicinity of the BNBT/BCZT interface, where BNBT experiences an elongation along the OOP direction. Furthermore, the BNBT and BCZT peaks are defused within the area in which their boundaries merge with each other. This

effect could be due to a region of substantial chemical intermixing at the BNBT/BCZT interface.

High-resolution aberration-corrected STEM measurements were carried out to study the interdiffusion of elements and their coupling at the interface. Figure 2a,b shows a high-angle annular dark-field (HAADF) and fast Fourier transform images, respectively, to illustrate the interfacial structure in the BNBT<sub>200</sub>/BCZT<sub>200</sub> bilayer. Sets of electron-diffraction spots, arising from the BNBT, BCZT, and the STO substrate, respectively, can be unambiguously indexed based on the crystal structure (Figure 2c). This pattern clearly exhibits the orientation sequence [001]BNBT//[001]BCZT//[001]-LSMO//[001]STO. A semicoherent-like interface is often observed in oxide heterostructures and epitaxially strained oxide films, where the growth environment can lead to the nucleation of extended defects such as misfit dislocations and stacking faults.<sup>16–20</sup> These defect structures can be attributed to the interdiffusion of cations across the BNBT and BCZT layers.

In fact, STEM-EDS mapping performed at the interface confirms the intermixing and diffusion of some elements (Figure 2d,e). In particular, Ba, Ca, and Zr (from BCZT) diffuse up to  $\sim 5$  nm into the BNBT layer, whereas Bi and Na (from BNBT) diffuse up to  $\sim 8$  nm into the BCZT layer. By performing numerical integration of the STEM-EDS data, we estimate that chemical intermixing leads to an average bound charge,  $\sigma_{int}$ , of 2.2  $\mu\text{C}/\text{cm}^2$  at the BNBT<sub>200</sub>/BCZT<sub>200</sub> interface (further experimental evidence of the existence of  $\sigma_{int}$  will be presented later on in this section).

**Electrocaloric Measurement.** Room-temperature  $P$ - $E$  hysteresis loops of all the samples measured at 1 kHz with an applied electric field of 620 kV/cm are shown in Figure S2. The saturation polarization ( $P_s$ ) of BNBT<sub>400</sub> and BCZT<sub>400</sub> monolayers are 47.6 and 16.6  $\mu\text{C}/\text{cm}^2$ , respectively, whereas all the BNBT/BCZT bilayers present intermediate  $P_s$  values.

Table 1. Maximum  $\Delta T^a$ 

EC materials	T (K)	$ \Delta T $ (K)	$ \Delta S $ (J/kgK)	$\Delta E$ (kV/cm)	$ Q $ (J/kg)	$ \Delta T/\Delta E $ (K cm/kV)	ref.
Lead-Based Materials							
0.9PMN-0.1PT (B)	298	0.23		105		0.0022	21
0.70PMN-0.30PT (B)	429	2.7	2.3	90	6.21	0.03	22
PbZr <sub>0.455</sub> Sn <sub>0.455</sub> Ti <sub>0.09</sub> O <sub>3</sub> (B)	317	1.6	1.8	30	54	0.0533	23
0.93PMN-0.07PT (F)	298	9	11	723	99	0.012	24
PbZrO <sub>3</sub> (F)	508	11.4		510		0.022	25
(Pb <sub>0.97</sub> La <sub>0.02</sub> )(Zr <sub>0.95</sub> Ti <sub>0.05</sub> )O <sub>3</sub> (F)	210	8.5		1110		0.008	26
PbZr <sub>0.95</sub> Ti <sub>0.05</sub> O <sub>3</sub> (F)	499	12	8	776	96	0.015	10
PbZr <sub>0.52</sub> Ti <sub>0.48</sub> O <sub>3</sub> (F)	659	11.1	6.17	577	68.49	0.0192	27
Polymer-Based Materials (F)							
P(VDF-TrFE) 68/32 mol %	306	20	95	1600	1900	0.0125	28
P(VDF-TrFE-CFE)	303	15	80	1500	1200	0.011	29
P(VDF-TrFE)/BST75	352	2.5		600		0.0042	30
Terpolymer/PMN-PT	303	31		1800		0.017	31
P(VDF-TrFE) 55/45 mol %	353	12	56	2090	672	0.0057	11
Lead-Free Materials							
BaZr <sub>0.2</sub> Ti <sub>0.8</sub> O <sub>3</sub> (B)	313	4.5	8	145	36	0.031	32
SrTiO <sub>3</sub> (B)	17	0.06		70		0.0008	33
Na <sub>0.5</sub> Bi <sub>0.5</sub> TiO <sub>3</sub> (B)	412	0.33	0.45	50	0.1485	0.0066	34
Ba <sub>0.65</sub> Sr <sub>0.35</sub> Ti <sub>0.997</sub> Mn <sub>0.003</sub> O <sub>3</sub> (B)	293	3.1	4.8	130	14	0.023	35
BaTiO <sub>3</sub> (F)	353	7.1	10.1	800	71.71	0.0089	36
SrBiTa <sub>2</sub> O <sub>9</sub> (F)	560	4.93	2.4	600	14	0.008	37
BNBT/BCZT bilayer (F)	370	23	26.1	620	600.3	0.037	this work

<sup>a</sup>Maximum  $\Delta T$  observed at a temperature ( $T$ ), adiabatic temperature change ( $\Delta T$ ), isothermal entropy change ( $\Delta S$ ), applied electric field ( $\Delta E$ ), isothermal heat, i.e., refrigerant capacity ( $Q = \Delta T\Delta S$ ), electrocaloric coefficient ( $\Delta T/\Delta E$ ) of typical ferroelectric materials. \*Bulk (B) and Film (F).

Temperature-dependent  $P$ - $E$  loops were measured to assess the corresponding ECE responses through the indirect method (Figure 3 and Figures S3–S6). On the basis of the Maxwell relation  $\left(\frac{\partial P}{\partial T}\right)_E = \left(\frac{\partial S}{\partial T}\right)_E$ , the electrocaloric adiabatic temperature,  $\Delta T_{\text{ECE}}$ , and isothermal entropy,  $\Delta S_{\text{ECE}}$ , changes can be estimated indirectly as<sup>1,10</sup>

$$\Delta T_{\text{ECE}} = -\frac{T}{C_p \rho} \int_0^{E_{\text{max}}} \left(\frac{\partial P}{\partial T}\right)_E dE \quad (1)$$

$$\Delta S_{\text{ECE}} = \frac{1}{\rho} \int_0^{E_{\text{max}}} \left(\frac{\partial P}{\partial T}\right)_E dE \quad (2)$$

where  $C_p$  is the heat capacity,  $\rho$  is the density of the material,  $P$  is the polarization, and  $E_{\text{max}}$  is the maximum applied electric field. The numerical values of  $(\partial P/\partial T)_E$  were obtained from seventh-order polynomial fits to the  $P$ - $T$ - $E$  plots, and our ECE results are reported in Figure 3.

The maxima of  $\Delta T_{\text{ECE}}$  and  $\Delta S_{\text{ECE}}$  span over a relatively broad temperature range, which can be ascribed to the fact that none of the bilayer samples shows sharp phase transitions (Figure S7). The maximum in  $\Delta T_{\text{ECE}}$  appears at 358–372 K, which is electric field and sample composition dependent. The maximum  $\Delta T_{\text{ECE}}$  estimated for BNBT<sub>400</sub> and BCZT<sub>400</sub> is 4.8 and 2.3 K, respectively, and the corresponding  $\Delta S_{\text{ECE}}$  to -5.3 and -2.6 J/kgK. Remarkably, the bilayer samples show a huge enhancement in  $\Delta T_{\text{ECE}}$  and  $\Delta S_{\text{ECE}}$ . Specifically, the BNBT<sub>200</sub>/BCZT<sub>200</sub> bilayer displays  $\Delta T_{\text{ECE}} = \sim 23$  K and  $\Delta S_{\text{ECE}} = -26.1$  J/kgK (for  $E = 620$  kV/cm), which are the highest in absolute value among all the investigated samples. To the best of our knowledge, the  $\Delta T_{\text{ECE}}$  measured indirectly in BNBT<sub>200</sub>/BCZT<sub>200</sub> constitutes a record among all the lead-free oxide perovskite and polymeric materials reported to date (Table 1). As we explain next, the origin of the giant ECE effect measured

in BNBT/BCZT bilayers cannot be explained solely in terms of enhanced internal electric fields in the individual layers.<sup>38</sup>

**Theoretical Model and Calculations.** To qualitatively understand the origin of the giant electrocaloric effects disclosed in BNBT/BCZT bilayers, we employ a theoretical approach similar to that described in ref 39. This approach takes into account the ferroelectric behavior of each individual layer as well as the electrostatic coupling between them. In particular, the total energy of the bilayer thin film systems is expressed as

$$U_{\text{tot}}(D, T, \lambda, E) = \lambda U_{\text{BNBT}}(D, T, E) + (1 - \lambda) U_{\text{BCZT}}(D, T, E) \quad (3)$$

where  $\lambda$  represents the relative mass content of BNBT,  $T$  is the temperature,  $U$  is the energy of each layer,  $D$  is the electric displacement along the direction perpendicular to the bilayer interface (which can be reasonably approximated by the electric polarization  $P$  in that direction, namely,  $D \approx P$ ), and  $E$  is the external electric field (also applied along the direction perpendicular to the bilayer stacking plane). By construction, eq 3 enforces continuity of the electric displacement along the bilayer stacking direction, as it is required by fundamental reasons.

The energy of each layer has been approximated by a Taylor expansion of the free energy in the electric displacement, specifically

$$U_A(D, T, E) = U_0 + \alpha_0(T - T_c)D^2 + \frac{1}{2}\beta D^4 - \left(\frac{1}{\Omega_0}\right)ED \quad (4)$$

where  $U_0$  is an arbitrary energy constant,  $T_c$  represents the ferroelectric to the paraelectric transition temperature of layer  $A$ , and  $\alpha_0$  and  $\beta$  are positively defined constants describing the

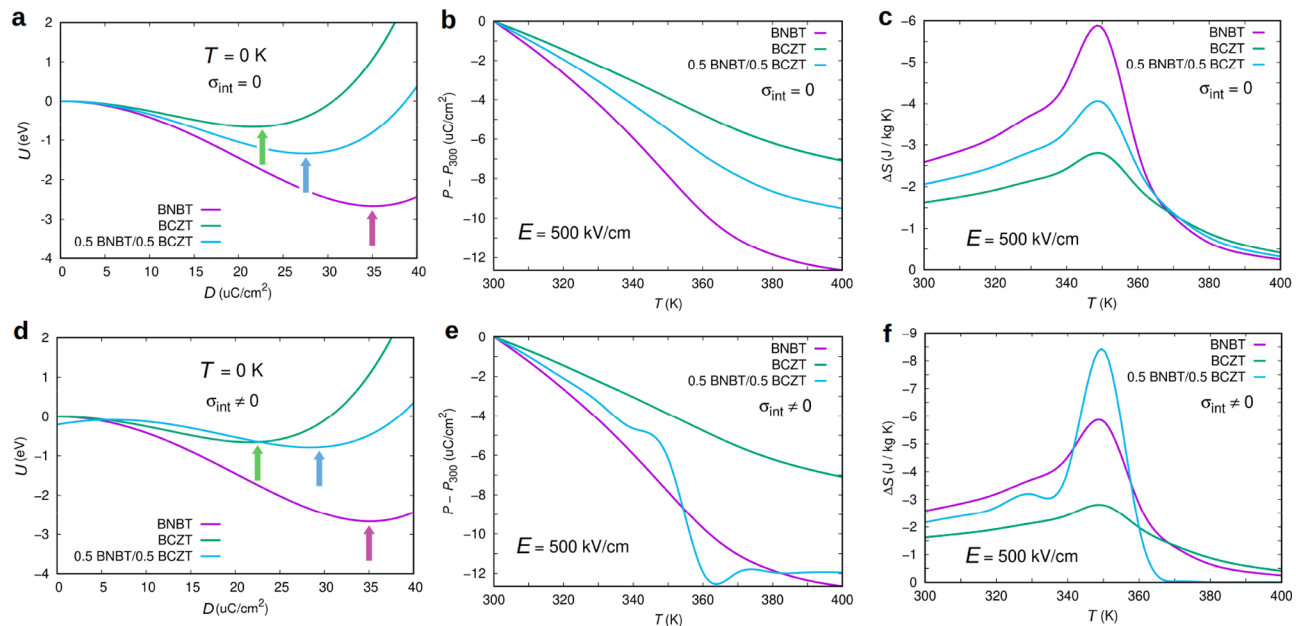


**Figure 4.** Theoretical calculations for single-domain bulk BNBT, bulk BCZT, and a 0.5 BNBT/0.5 BCZT bilayer considering different temperature conditions and an arbitrary maximum electric field of 500 kV/cm. (a–c) Results obtained for a null interface charge and (d–f) for  $\sigma_{\text{int}} = 4 \mu\text{C cm}^{-2}$  (i.e., the same order of magnitude than determined experimentally). Colored arrows in (a,d) indicate spontaneous electric polarizations.

ferroelectric/dielectric behavior of the system; the last term in eq 4 describes the interaction of the dielectric material with the external electric bias, where  $\Omega_0$  is the volume of the layer.

We have performed a series of first-principles calculations based on density functional theory to determine the value of  $\alpha_0$  and  $\beta$  for bulk BNBT and BCZT (Methods). The corresponding ferroelectric transition temperatures have been adopted close to their experimental values ( $T_c = 350$  K).<sup>40,41</sup> For a given  $\lambda$ ,  $T$ , and  $E$ , the equilibrium electric displacement, or equivalently, electric polarization  $P$ , of the bilayer can be determined straightforwardly by finding the minimum of  $U_{\text{tot}}$  (see arrows in Figures 4a). By applying this approach repeatedly over a dense grid of  $\lambda$ ,  $T$ , and  $E$  data points, one can estimate the adiabatic entropy change associated with the electrocaloric effect with the well-known formula

$$\Delta S_\lambda(T, E) = \int \frac{\partial P_\lambda(T, E')}{\partial T \partial E'} dE' \quad (5)$$

In the presence of chemical intermixing at the bilayer interface, a net-bound charge of compositional origin,  $\sigma_{\text{int}}$ , should appear therein.<sup>39,42</sup> In that case, eq 3 needs to be modified as follows in order to fulfill Maxwell fundamental equations

$$U_{\text{tot}}(D, T, \lambda, E, \sigma_{\text{int}}) = \lambda U_{\text{BNBT}}(D, T, E) + (1 - \lambda) U_{\text{BCZT}}(D - \sigma_{\text{int}}, T, E) \quad (6)$$

Analogously to the null interface-charge case, now one can determine the electric polarization of the system as a function of composition, temperature, electric field, and  $\sigma_{\text{int}}$ , namely,  $P_\lambda(T, E, \sigma_{\text{int}})$ , as well as the accompanying adiabatic entropy change,  $\Delta S_\lambda(T, E, \sigma_{\text{int}})$ .

The theoretical model explained above has been used to simulate the electrocaloric behavior of a BNBT<sub>200</sub>/BCZT<sub>200</sub> ( $\lambda = 0.5$ ) thin-film bilayer. The  $\Delta S$  results calculated as a function of interface charge, temperature, and applied electric fields are

shown in Figure 4c,f. When the interface charge is assumed to be zero (i.e., case corresponding to no chemical intermixing), it is found that the electrocaloric response of the bilayer corresponds to a certain average between the two limiting cases BNBT and BCZT. Certainly, the internal electric fields in the individual layers of the bilayer, which are proportional to the energy derivatives  $\partial U_{\text{BNBT}}/\partial D$  and  $\partial U_{\text{BCZT}}/\partial D$ , are locally not zero and can be large due to the continuity of the electric displacement along the bilayer stacking direction<sup>38</sup> and differences in dielectric properties (Figures S2 and S7). However, the total  $|\Delta S|$  of the bilayer never surpasses (falls below) the maximum adiabatic entropy change estimated for the BNBT (BCZT) thin film at  $T_c$  (Figure 4c). In particular, a maximum  $\Delta S$  of  $\sim -4$  J/kg K is computed for the bilayer whereas  $\sim -6$  J/kg K ( $\sim -2$  J/kg K) for the BNBT (BCZT) monolayer. Consistently, the  $T$ -induced variation of the bilayer polarization is smaller (larger) than estimated for BNBT (BCZT) under same  $T$  and  $E$  conditions (see Figure 4b and eq 1).

When a certain bound interface charge is present in the bilayer (i.e., chemical intermixing at the bilayer interface), the electrocaloric response of the system changes substantially. Specifically, the maximum adiabatic entropy change of the bilayer now becomes larger in absolute value than calculated for the BNBT and BCZT thin films (Figure 4f). For instance, a maximum  $\Delta S$  of  $\sim -8.5$  J/kgK is obtained for the bilayer at  $T_c = 350$  K, which is considerably larger than the values estimated for the two layers separately. The reasons for this outcome are the changes caused by  $\sigma_{\text{int}}$  on the dielectric properties of the bilayer (Figure 4d and Figure S8) in which a higher number of polar competing phases appear.<sup>39</sup> In particular, a state with a quite small spontaneous polarization gets stabilized in the bilayer at conditions  $T > T_c$  and  $E \neq 0$ , which remained metastable at lower temperatures (Figure S8).<sup>39</sup> Consequently, as it is appreciated in Figure 4e, an abrupt variation in the bilayer polarization occurs at  $T \approx T_c$  in contrast to what is

observed for BNBT and BCZT where  $P$  varies more smoothly with temperature.

The theoretical results obtained with our simple but physically correct model indicate that the likely cause for the enhanced electrocaloric effect observed in BNBT<sub>200</sub>/BCZT<sub>200</sub> is the presence of a net-bound charge at their interface. In the absence of interface charges, the electrocaloric response of the bilayer always lies between those of BNBT and BCZT. The maximum entropy change induced by an electric field depends strongly on  $\sigma_{\text{int}}$  hence one may be able to tune the electrocaloric response of bilayers by means of interface engineering.

**KPFM and PFM Measurements.** Kelvin probe force microscopy (KPFM) measurements were carried out to measure the surface potential ( $V_{\text{sp}}$ ) of the devices, which is sensitive to the surface charges and work function  $\Phi$  of the materials. The morphology of the cross-section of the devices unambiguously reflects the bilayer structure of the BNBT<sub>200</sub>/BCZT<sub>200</sub> with the thickness of individual layer around  $\sim 200$  nm. Figure 5b maps the corresponding surface potential and the specific line profile was shown in Figure 5c. The large variation of  $V_{\text{sp}}$  when tip crossing the BNBT/BCZT interface indicates the presence of an internal field throughout the two

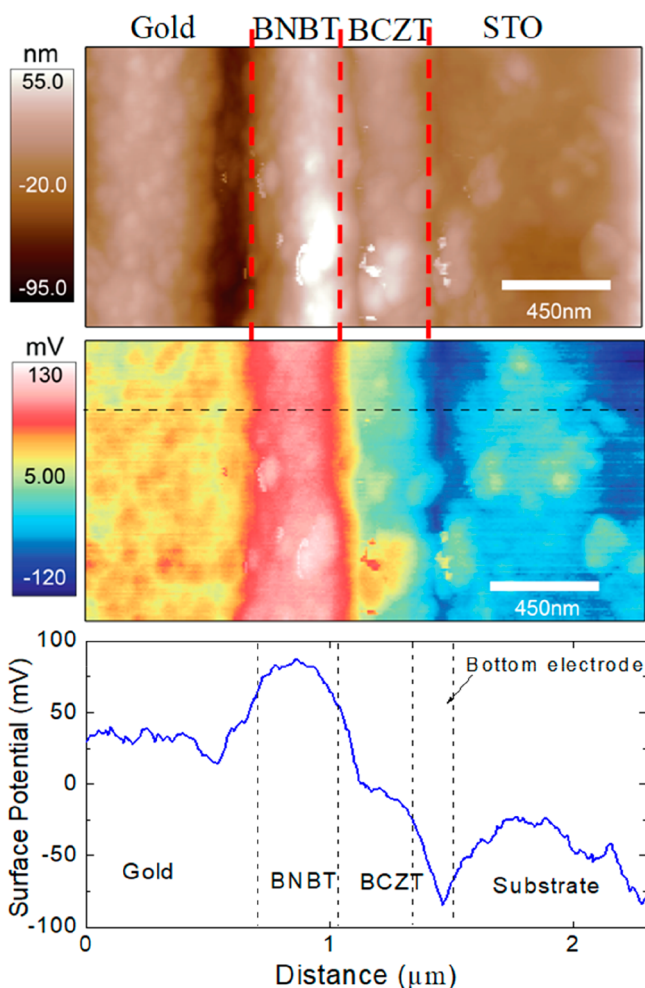


**Figure 5.** Cross-sectional surface potential for BNBT<sub>200</sub>/BCZT<sub>200</sub> bilayer thin film measured by KPFM. (a) Surface morphology of cross-section. (b) Surface potential image. (c) Surface potential profiles obtained from image (b).

thin-films ( $E = -dV_{\text{sp}}/dx$ ). The direction of this  $E$ -field points from the BNBT film toward the BCZT film, which will induce the prealignment of the spontaneous polarization in both thin films before exposed to the external  $E$ -field.

Further piezoelectric force microscope (PFM) measurements were carried out to strengthen the support to the existence of the built-in electric field. Figure 6a shows the temperature-dependent local switching spectroscopy amplitude–voltage butterfly loops of the BNBT<sub>200</sub>/BCZT<sub>200</sub> bilayer. Measurements were carried out by applying  $\pm 20$  V along the OOP direction. These butterfly loops become more asymmetric at high temperature (namely, a sharp decrease in amplitude appears for negative voltages at  $>370$  K). The negative voltage offset on the amplitude–voltage butterfly loops and the phase–voltage hysteresis loops (Figure 6a,b) are consistent with the macroscopic  $P$ – $E$  hysteresis loop measurement, which can be ascribed to the presence of a built-in electric field and/or trapped charges at the interface.<sup>43,44</sup> The surface potential mapping indicates that the built-in  $E$ -field will favor the downward alignment of the  $P$  in both BNBT and BCZT thin films, which suggest that higher negative bias are required to switch the dipole moment upward. The consistency of the macroscopic  $P$ – $E$  hysteresis loop, KPFM, and PFM measurements pointing toward the existence of  $\sigma_{\text{int}}$  in the bilayer, even though the vertical shift of the phase–voltage hysteresis loops along the response axis can be related to the asymmetric electrode structure and imprint process<sup>45</sup> among other possibilities.<sup>46,47</sup> Piezoresponse (Figure 6c) was extracted from both the phase–voltage hysteresis loop and amplitude loop with the simple harmonic oscillator (SHO) model fitting to determine the temperature-dependent piezoresponse behavior of BNBT/BCZT bilayer.<sup>48</sup>

**Discussion.** The measured giant adiabatic temperature and isothermal entropy spans convert multilayered oxide heterostructures into very attractive electrocaloric (EC) materials. Table 1 offers a comparison in terms of cooling performance between BNBT/BCZT bilayers and other promising EC compounds. First, the operating temperature of BNBT/BCZT bilayers is near room temperature and the corresponding maximum  $\Delta T$  represents a new record among all the lead-free inorganic EC materials reported to date. Second, the electric fields required in BNBT/BCZT bilayer ( $E \sim 600$  kV/cm) are much smaller than in ferroelectric polymers ( $E > 1500$  kV/cm), for example, whereas similar  $\Delta T$  values are obtained in both cases. Certainly, in terms of the electrocaloric strength, which is defined as  $|\Delta T/\Delta E|$ , BNBT/BCZT bilayers emerge as particularly promising: only BZT<sup>32</sup> and other few lead-based perovskites display comparable figures (i.e.,  $|\Delta T/\Delta E| > 0.03$  K cm/kV). In this sense, it can be said that BNBT/BCZT bilayers unite the best of the ferroelectric ceramics and ferroelectric polymer worlds. We should note that the design rule behind the giant ECE disclosed in this work, namely, tuning of compositional bound interface charges in thin-film bilayers, should work equally well for other possible combinations of ferroelectric materials. Hence, our work brings new exciting prospects to the field of solid-state cooling based on a well-known concept: interface engineering.<sup>14,15</sup>

In summary, we have disclosed a new design of lead-free ferroelectric materials based on thin-film bilayers and bound interface charges that maximizes drastically the size of electrocaloric effects. A giant primary electrocaloric effect of  $\Delta T_{\text{ECE}} = \sim 23$  K has been observed at  $T \sim 375$  K in a BNBT<sub>200</sub>/BCZT<sub>200</sub> thin-film bilayer grown on an STO(001)

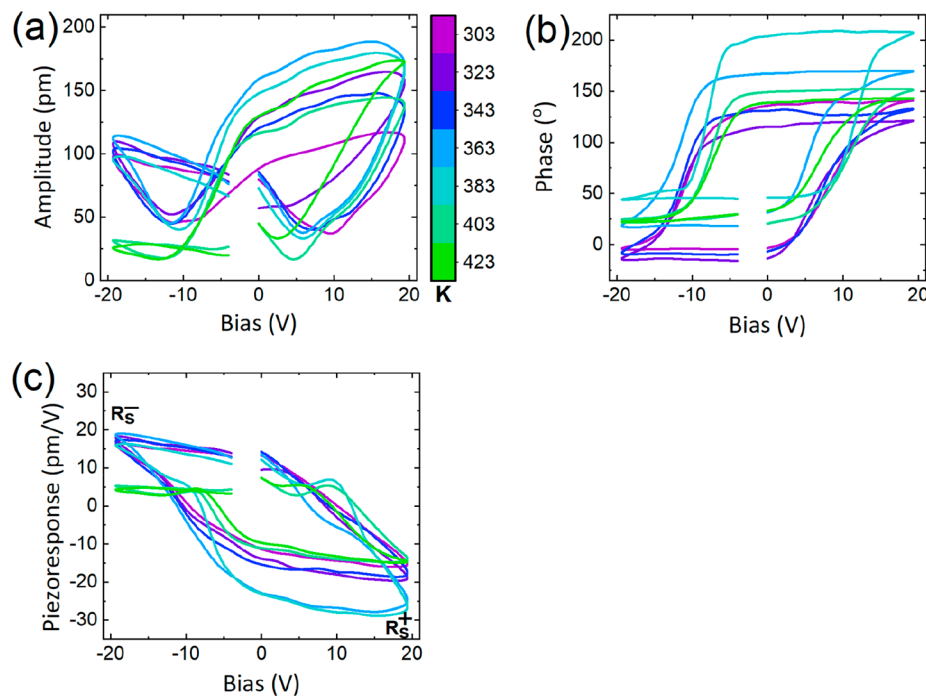


**Figure 6.** PFM measurements at different temperatures. (a) Amplitude–voltage butterfly loops. (b) Phase–voltage hysteresis loops. (c) Temperature dependence of piezoresponse against voltage after SHO fitting.

substrate. STEM-EDS, KPFM, and PFM measurements reveal the presence of chemical intermixing and bound charges at the bilayer interface, which plays a major role in the enhancement of the electrocaloric response of the material. This effect has been confirmed by our bilayer model calculations which explicitly take into account the electrostatic coupling and dielectric changes caused by interfacial bound charges. The overall  $\Delta T$  measured in the  $\text{BNBT}_{200}/\text{BCZT}_{200}$  thin-film bilayer represents a new record among all the lead-free inorganic electrocaloric materials reported to date. Our work proves the great potential of multilayered oxide heterostructures in which interface engineering may lead to novel ferroelectric states and functionalities for developing highly efficient, environmentally friendly, and highly scalable solid-state refrigeration devices.

**Methods. Experimental Section.** The bilayer thin film is composed of two ferroelectric layers with different thickness sandwiched between electrodes, which are in series with each layer as schematically illustrated in Figure S1. Epitaxial  $\text{BNBT}_{400}$ ,  $\text{BNBT}_{300}/\text{BCZT}_{100}$ ,  $\text{BNBT}_{200}/\text{BCZT}_{200}$ ,  $\text{BNBT}_{40}/\text{BCZT}_{360}$ , and  $\text{BCZT}_{400}$  (the subscript refers to the thin-film thickness in nm) bilayer thin films were deposited on  $\text{SrTiO}_3$  (STO) (001) single crystal substrate by laser molecular beam epitaxy (LMBE). Conductive  $\text{La}_{0.7}\text{Sr}_{0.3}\text{MnO}_3$  (LSMO) was used as lattice matched bottom electrodes. The total thickness of the bilayers was kept at  $\sim 400$  nm. A KrF excimer laser (248 nm) with an energy density of  $2 \text{ J/cm}^2$  was adopted for the deposition. The growth of BNBT, BCZT, and LSMO layers was carried out at a substrate temperature of 750, 850, and 800  $^\circ\text{C}$ , respectively, under an oxygen partial pressure of 200 mTorr using ceramic targets of respective materials. The trace amount of Mn (0.5 mol %) was introduced into the BNBT target to reduce the leakage current in the resulted thin films. The repetition rate of the laser was kept at 5 Hz and the distance between the targets and substrates was fixed at 5 cm.

The leakage current density versus electric field curves ( $I$ – $V$ ) of  $\text{BZCT}/\text{BNBT}$  bilayer at various temperatures are characterized using the Radiant Precision Multiferroic Tester Unit (Radiant Technologies) connected with a temperature-controlled sample stage (Linkam HFS600E-PB4).

The crystallographic structure was characterized by X-ray diffraction (XRD, MRD (PANalytical) Xpert Materials Research diffractometer) with  $\text{Cu K}\alpha$  radiation and (220) Ge monochromators. The cross-sectional interfacial structure was observed by an aberration-corrected JEOL JEMARM200F transmission electron microscopy (TEM). The cross-sectional TEM specimens were prepared using focused ion beam milling, followed by thinning with Ar ion milling. The same TEM instrument with a point resolution of less than 0.08 nm was used for the energy-dispersive X-ray spectroscopy (EDS) element mapping. The temperature-dependent dielectric permittivity curves of all the samples are obtained using an Agilent E4980A LCR meter with a temperature-controlled chamber (Linkam HFS600E).  $P$ – $E$  hysteresis loops were measured by Radiant precision workstation (Radiant Technologies, Albuquerque, NW) at a frequency of 1 kHz at different temperatures. Using the  $P$ – $E$  loops measured at different temperatures we estimate the  $\Delta T$  and  $\Delta S$  by the indirect method.

The temperature-dependent PFM and KPFM measurements were carried out on a commercial atomic force microscope (Cypher, AFM, Asylum Research) with the environmental scanner (Asylum Research). Pt/Ir-coated conductive Si probes with the calibrated spring constant  $k \sim 2.49 \text{ N/m}$  and resonance frequency  $f \sim 75 \text{ kHz}$  (PPP-EFM, nanosensors) was used with loading forces  $\sim 180 \text{ nN}$ . In order to minimize the cross-talks with the morphology, all the PFM measurements were conducted under the dual alternating current (ac) resonance tracking (DART) mode. For the switching spectroscopy measurement (SSPFM), a small ac signal near the resonance frequency ( $V_{\text{ac}} \sim 0.5 \text{ V}$ , near 310 kHz) was

superimposed on a 0.2 Hz triangular staircase wave. Both the writing and reading times are 25 ms and the bias window was around 20 V. The measured amplitude was analyzed using a simple harmonic oscillator (SHO) fit to extract the piezo-response, resonant frequency, and quality factor ( $Q$ -factor). For the KPFM measurement, a gold layer of  $\sim 1 \mu\text{m}$  thick was deposited on the surface of bilayer thin films to prevent tip crashes during the cross-sectional KPFM scanning. The two-pass method was adopted for the topography and electrical potential, respectively. The first pass was the standard ac mode imaging with the tip oscillation amplitudes  $\sim 28 \text{ nm}$ . With the tip lifted up by 10 nm, the second pass measured the surface potential by applying both ac and direct current (dc) voltage on the tip. During the measurement, both the Au and LSMO electrodes are grounded.

**First-Principles Calculations.** First-principles calculations based on density functional theory (DFT) were performed to estimate the value of the parameters  $\alpha_0$  and  $\beta$  entering the expression of the layer energy in eq 4. We employed the PBE variant of the generalized gradient approximation to DFT<sup>49</sup> as is implemented in the VASP package.<sup>50,51</sup> The projector augmented wave method is employed to represent the ionic cores,<sup>52</sup> and we considered the following electrons as valence: Na's 3s, and 2p; Bi's 5d, 6s, and 6p; Ti's 3p, 4s, and 3d; Ba's 5s, 5p, and 6s; Zr's 4s, 4p, 5s, and 4d; Ca's 3s, 3p, and 4s; and O's 2s and 2p. Wave functions were represented in a plane-wave basis truncated at 650 eV, and we used a 40-atoms simulation cell (equivalent to a  $2 \times 2 \times 2$  replication of the typical 5-atom perovskite unit cell) that allows one to reproduce the usual ferroelectric and antiferro distortive distortions occurring in oxide compounds.<sup>53,54</sup> For integrations within the first Brillouin zone, we adopted a Gamma-centered  $k$ -point grid of  $8 \times 8 \times 8$ . Geometry relaxations were performed by using a conjugate-gradient algorithm that changed the volume and shape of the unit cell. The imposed tolerance on the atomic forces was of  $0.01 \text{ eV} \cdot \text{\AA}^{-1}$ . By using these technical parameters, we obtain total energies that are converged to within 0.5 meV per formula unit (f.u.).

The energy and electric polarization of the high-symmetry high- $T$  cubic (nonpolar  $Pm\bar{3}m$ ) and low-symmetry low- $T$  monoclinic (polar  $R3c$ ) phases of bulk BNBT and BCZT were calculated in order to determine the value of the parameters  $\alpha_0$  and  $\beta$ . Our calculations render  $\alpha_0 = 1.236 \times 10^{-5} \text{ eV cm}^4 \text{ K}^{-1} \mu\text{C}^{-2}$  and  $\beta = 1.754 \times 10^{-6} \text{ eV cm}^8 \mu\text{C}^{-4}$  for BNBT, and  $\alpha_0 = 8.012 \times 10^{-6} \text{ eV cm}^4 \text{ K}^{-1} \mu\text{C}^{-2}$  and  $\beta = 2.997 \times 10^{-6} \text{ eV cm}^8 \mu\text{C}^{-4}$  for BCZT. According to our DFT calculations,<sup>53</sup> the spontaneous polarization of bulk BNBT and BCZT at zero temperature amounts to 35.12 and 21.63  $\mu\text{C cm}^{-2}$ , respectively. In our bilayer model calculations, we employed a finite  $\sigma_{\text{int}}$  value of 4  $\mu\text{C cm}^{-2}$ , which is the same order of magnitude than estimated experimentally from the STEM-EDS data.

## ■ ASSOCIATED CONTENT

### ■ Supporting Information

The Supporting Information is available free of charge at <https://pubs.acs.org/doi/10.1021/acs.nanolett.9b04727>.

Schematic illustration of BNBT/BCZT bilayer thin films, room-temperature polarization versus electric field ( $P$ - $E$ ) hysteresis loops, EC results of BCZT<sub>400</sub>, BNBT<sub>40</sub>/BCZT<sub>360</sub>, BNBT<sub>300</sub>/BCZT<sub>100</sub> and BNBT<sub>400</sub> samples, relative permittivity ( $\epsilon_r$ ) versus temperature

plots measured at 1 kHz, theoretical calculations for single-domain bulk BNBT, bulk BCZT, and a 0.5 BNBT/0.5 BCZT bilayer, PFM measurements at different temperatures, the leakage current density versus voltage curves ( $I$ - $V$ ) of BCZT<sub>200</sub>/BNBT<sub>200</sub> bilayer thin film (PDF)

## ■ AUTHOR INFORMATION

### Corresponding Author

\*E-mail: [dy.wang@unsw.edu.au](mailto:dy.wang@unsw.edu.au).

### ORCID

Sagar E. Shirsath: 0000-0002-2420-1144

Claudio Cazorla: 0000-0002-6501-4513

Yun Liu: 0000-0002-5404-3909

Danyang Wang: 0000-0002-7883-8001

### Notes

The authors declare no competing financial interest.

## ■ ACKNOWLEDGMENTS

Financial supports from the Australian Research Council (DP170103514, FT180100541) are acknowledged by D.W., and Australian Research Council (FT140100135) is acknowledged by C.C.. This work was performed in part at the New South Wales node of the Australian National Fabrication Facility, a company established under the National Collaborative Research Infrastructure Strategy to provide nano- and microfabrication facilities for Australia's researchers. The authors thank Dr. C. Kong and Dr. R. Webster for technical assistance in preparing TEM sample and use of facilities supported by Microscopy Australia at the Electron Microscope Unit at UNSW.

## ■ REFERENCES

- (1) Pecharsky, V. K.; Gschneidner, K. A., Jr. Giant magnetocaloric effect in  $\text{Gd}_5(\text{Si}_2\text{Ge}_2)$ . *Phys. Rev. Lett.* **1997**, *78*, 4494.
- (2) Bonnot, E.; Romero, R.; Mañosa, L.; Vives, E.; Planes, A. Elastocaloric effect associated with the martensitic transition in shape-memory alloys. *Phys. Rev. Lett.* **2008**, *100*, 125901.
- (3) Aznar, A.; Lloveras, P.; Romanini, M.; Barrio, M.; Tamarit, J. L.; Cazorla, C.; Errandonea, D.; Mathur, N. D.; Planes, A.; Moya, X.; et al. Giant barocaloric effects over a wide temperature range in superionic conductor AgI. *Nat. Commun.* **2017**, *8*, 1851.
- (4) Sagotra, A. K.; Chu, D.; Cazorla, C. Room-temperature mechanocaloric effects in lithium-based superionic materials. *Nat. Commun.* **2018**, *9*, 3337.
- (5) Scott, J. F. Electrocaloric Materials. *Annu. Rev. Mater. Res.* **2011**, *41*, 229–240.
- (6) Defay, E.; Crossley, S.; Kar-Narayan, S.; Moya, X.; Mathur, N. D. The electrocaloric efficiency of ceramic and polymer films. *Adv. Mater.* **2013**, *25*, 3337–3342.
- (7) Kar-Narayan, S.; Mathur, N. D. Direct and indirect electrocaloric measurements using multilayer capacitors. *J. Phys. D: Appl. Phys.* **2010**, *43*, 032002.
- (8) Geng, W. P.; Liu, Y.; Meng, X. J.; Bellaiche, L.; Scott, J. F.; Dkhil, B.; Jiang, A. Q. Giant negative electrocaloric effect in antiferroelectric La-doped  $\text{Pb}(\text{ZrTi})\text{O}_3$  thin films near room temperature. *Adv. Mater.* **2015**, *27*, 3165–3169.
- (9) Defay, E.; Faye, R.; Despesse, G.; Strozyk, H.; Sette, D.; Crossley, S.; Moya, X.; Mathur, N. D. Enhanced electrocaloric efficiency via energy recovery. *Nat. Commun.* **2018**, *9*, 1827.
- (10) Mischenko, A. S.; Zhang, Q.; Scott, J. F.; Whatmore, R. W.; Mathur, N. D. Giant Electrocaloric Effect in Thin-Film  $\text{PbZr}_{0.95}\text{Ti}_{1.05}\text{O}_3$ . *Science* **2006**, *311*, 1270.

- (11) Neese, B.; Chu, B.; Lu, S.-G.; Wang, Y.; Furman, E.; Zhang, Q. Large Electrocaloric effect in ferroelectric polymers near room temperature. *Science* **2008**, *321*, 821–823.
- (12) Asbani, B.; Gagou, Y.; Dellis, J.-L.; Trcek, M.; Kutnjak, Z.; Amjoud, M.; Lahmar, A.; Mezzane, D.; El Marsi, M. Lead-free  $\text{Ba}_{0.8}\text{Ca}_{0.2}\text{Te}_x\text{Ti}_{1-x}\text{O}_3$  ferroelectric ceramics exhibiting high electrocaloric properties. *J. Appl. Phys.* **2017**, *121*, 064103.
- (13) Kutnjak, Z.; Rožič, B.; Pirc, R. Electrocaloric effect: theory, measurements, and applications. *Wiley Encyclopedia of electrical and electronics engineering*; John Wiley & Sons, Inc, 2015; pp 1–19.
- (14) Zubko, P.; Gariglio, S.; Gabay, M.; Ghosez, P.; Triscone, J.-M. Interface physics in complex oxide heterostructures. *Annu. Rev. Condens. Matter Phys.* **2011**, *2*, 141–165.
- (15) Yu, P.; Chu, Y.-H.; Ramesh, R. Oxide interfaces: pathways to novel phenomena. *Mater. Today* **2012**, *15*, 320–327.
- (16) Hirth, J. P.; Wang, J.; Tomé, C. N. Disconnections and other defects associated with twin interfaces. *Prog. Mater. Sci.* **2016**, *83*, 417.
- (17) Nakagawa, N.; Hwang, H. Y.; Muller, D. A. Why some interfaces cannot be sharp. *Nat. Mater.* **2006**, *5*, 204–209.
- (18) Ramesh, R.; Schlom, D. G. Creating emergent phenomena in oxide superlattices. *Nat. Rev.* **2019**, *4*, 257–268.
- (19) Huang, Z.; Ariando; Wang, X. R.; Rusydi, A.; Chen, J.; Yang, H.; Venkatesan, T. Interface engineering and emergent phenomena in oxide heterostructures. *Adv. Mater.* **2018**, *30*, 1802439.
- (20) Mundet, B.; Jareño, J.; Gazquez, J.; Varela, M.; Obradors, X.; Puig, T. Defect landscape and electrical properties in solution-derived  $\text{LaNiO}_3$  and  $\text{NdNiO}_3$  epitaxial thin films. *Phys. Rev. Lett.* **2018**, *2*, 063607.
- (21) Crossley, S.; Usui, T.; Nair, B.; Kar-Narayan, S.; Moya, X.; Hirose, S.; Ando, A.; Mathur, N. D. Direct electrocaloric measurement of 0.9 Pb  $(\text{Mg}_{1/3}\text{Nb}_{2/3})\text{O}_3$ -0.1  $\text{PbTiO}_3$  films using scanning thermal microscopy. *Appl. Phys. Lett.* **2016**, *108*, 032902.
- (22) Rožič, B.; Kosec, M.; Uršič, H.; Holc, J.; Malič, B.; Zhang, Q. M.; Blinc, R.; Pirc, R.; Kutnjak, Z. Influence of the critical point on the electrocaloric response of relaxor ferroelectrics. *J. Appl. Phys.* **2011**, *110*, 064118.
- (23) Thacher, P. Electrocaloric effects in some ferroelectric and antiferroelectric Pb (Zr, Ti)  $\text{O}_3$  compounds. *J. Appl. Phys.* **1968**, *39*, 1996–2002.
- (24) Correia, T. M.; Young, J. S.; Whatmore, R. W.; Scott, J. F.; Mathur, N. D.; Zhang, Q. Investigation of the electrocaloric effect in a  $\text{PbMg}_{1/3}\text{Nb}_{2/3}\text{O}_3$ - $\text{PbTiO}_3$  relaxor thin film. *Appl. Phys. Lett.* **2009**, *95*, 182904.
- (25) Parui, J.; Krupanidhi, S. Electrocaloric effect in antiferroelectric  $\text{PbZrO}_3$  thin films. *Phys. Status Solidi RRL* **2008**, *2*, 230–232.
- (26) Hao, X.; Yue, Z.; Xu, J.; An, S.; Nan, C.-W. Energy-storage performance and electrocaloric effect in (100)-oriented  $\text{Pb}_{0.97}\text{La}_{0.02}(\text{Zr}_{0.95}\text{Ti}_{0.05})\text{O}_3$  antiferroelectric thick films. *J. Appl. Phys.* **2011**, *110*, 064109.
- (27) Chukka, R.; Wei Cheah, J.; Chen, Z.; Yang, P.; Shannigrahi, S.; Wang, J.; Chen, L. Enhanced cooling capacities of ferroelectric materials at morphotropic phase boundaries. *Appl. Phys. Lett.* **2011**, *98*, 242902.
- (28) Lu, S. G.; Rožič, B.; Zhang, Q. M.; Kutnjak, Z.; Li, X.; Furman, E.; Gorny, L. J.; Lin, M.; Malič, B.; Kosec, M.; et al. Organic and inorganic relaxor ferroelectrics with giant electrocaloric effect. *Appl. Phys. Lett.* **2010**, *97*, 162904.
- (29) Li, X.; Qian, X.; Lu, S. G.; Cheng, J.; Fang, Z.; Zhang, Q. M. Unusual temperature dependence of electrocaloric effect in ferroelectric relaxor poly(vinylidene fluoride-trifluoroethylene-chlorofluoroethylene) terpolymer. *Appl. Phys. Lett.* **2011**, *99*, 052907.
- (30) Jiang, Z. Y.; Zheng, X. C.; Zheng, G. P. The enhanced electrocaloric effect in P(VDF-TrFE) copolymer with barium strontium titanate nano-fillers synthesized via an effective hydrothermal method. *RSC Adv.* **2015**, *5*, 61946–61954.
- (31) Huang, C.; Yang, H.-B.; Gao, C.-F. Giant electrocaloric effect in a cracked ferroelectrics. *J. Appl. Phys.* **2018**, *123*, 154102.
- (32) Qian, X.-S.; Ye, H. J.; Zhang, Y. T.; Gu, H.; Li, X.; Randall, C. A.; Zhang, Q. M. Giant Electrocaloric Response Over A Broad Temperature Range in Modified  $\text{BaTiO}_3$  Ceramics. *Adv. Funct. Mater.* **2014**, *24*, 1300–1305.
- (33) Hegenbarth, E. Studies of the electrocaloric effect of ferroelectric ceramics at low temperatures. *Cryogenics* **1961**, *1*, 242–243.
- (34) Bai, Y.; Zheng, G.-P.; Shi, S.-Q. Abnormal electrocaloric effect of  $\text{Na}_{0.5}\text{Bi}_{0.5}\text{TiO}_3$ - $\text{BaTiO}_3$  lead-free ferroelectric ceramics above room temperature. *Mater. Res. Bull.* **2011**, *46*, 1866–1869.
- (35) Liu, X. Q.; Chen, T. T.; Wu, Y. J.; Chen, X. M. Enhanced Electrocaloric Effects in Spark Plasma-Sintered  $\text{Ba}_{0.65}\text{Sr}_{0.35}\text{TiO}_3$ -Based Ceramics at Room Temperature. *J. Am. Ceram. Soc.* **2013**, *96*, 1021–1023.
- (36) Bai, Y.; Han, X.; Ding, K.; Qiao, L.-J. Combined effects of diffuse phase transition and microstructure on the electrocaloric effect in  $\text{Ba}_{1-x}\text{Sr}_x\text{TiO}_3$  ceramics. *Appl. Phys. Lett.* **2013**, *103*, 162902.
- (37) Chen, H.; Ren, T.-L.; Wu, X.-M.; Yang, Y.; Liu, L.-T. Giant electrocaloric effect in lead-free thin film of strontium bismuth tantalite. *Appl. Phys. Lett.* **2009**, *94*, 182902.
- (38) Zhang, T.; Li, W.; Cao, W.; Hou, Y.; Yu, Y.; Fei, W. Giant electrocaloric effect in PZT bilayer thin films by utilizing the electric field engineering. *Appl. Phys. Lett.* **2016**, *108*, 162902.
- (39) Cazorla, C.; Stengel, M. Ab initio design of charge-mismatched ferroelectric superlattices. *Phys. Rev. B: Condens. Matter Mater. Phys.* **2014**, *90*, No. 020101.
- (40) Keeble, D. S.; Benabdallah, F.; Thomas, P. A.; Maglione, M.; Kreisel, J. Revised structural phase diagram of  $(\text{Ba}_{0.7}\text{Ca}_{0.3}\text{TiO}_3)$ - $(\text{BaZr}_{0.2}\text{Ti}_{0.8}\text{O}_3)$ . *Appl. Phys. Lett.* **2013**, *102*, 092903.
- (41) Cordero, F.; Craciun, F.; Trequattrini, F.; Mercadelli, E.; Galassi, C. Phase transitions and phase diagram of the ferroelectric perovskite  $(\text{Na}_{0.5}\text{Bi}_{0.5})_{1-x}\text{Ba}_x\text{TiO}_3$  by an elastic and dielectric measurements. *Phys. Rev. B: Condens. Matter Mater. Phys.* **2010**, *81*, 144124.
- (42) Murray, E. D.; Vanderbilt, D. Influence of dielectric stiffness, interface, and layer thickness on hysteresis loops of ferroelectric superlattices. *Phys. Rev. B: Condens. Matter Mater. Phys.* **2009**, *79*, 100102.
- (43) Mangalam, R. V. K.; Karthik, J.; Damodaran, A. R.; Agar, J. C.; Martin, L. W. Unexpected crystal and domain structures and properties in compositionally graded  $\text{PbZr}_{(1-x)}\text{Ti}_x\text{O}_3$  thin films. *Adv. Mater.* **2013**, *25*, 1761–1767.
- (44) Lin, Q.; Wang, D.; Chen, Z.; Liu, W.; Lim, S.; Li, S. Periodicity dependence of the built-in electric field in  $(\text{Ba}_{0.7}\text{Ca}_{0.3})\text{TiO}_3/\text{Ba}(\text{Zr}_{0.2}\text{Ti}_{0.8})\text{O}_3$  ferroelectric superlattices. *ACS Appl. Mater. Interfaces* **2015**, *7*, 26301–26306.
- (45) Warren, W. L.; Dimos, D.; Pike, G. E.; Tuttle, B. A.; Raymond, M. V.; Ramesh, R.; Evans, J. T. Voltage shifts and imprint in ferroelectric capacitors. *Appl. Phys. Lett.* **1995**, *67*, 866.
- (46) Alexe, M.; Harnagea, C.; Hesse, D.; Gösele, U. Polarization imprint and size effects in mesoscopic ferroelectric structures. *Appl. Phys. Lett.* **2001**, *79*, 242.
- (47) Bhatia, B.; Karthik, J.; Cahill, D. G.; Martin, L. W.; King, W. P. High-temperature piezoresponse force microscopy. *Appl. Phys. Lett.* **2011**, *99*, 173103.
- (48) Proksch, R. In-situ piezoresponse force microscopy cantilever mode shape profiling. *J. Appl. Phys.* **2015**, *118*, 072011.
- (49) Perdew, J. P.; Burke, K.; Ernzerhof, M. Generalized Gradient Approximation Made Simple. *Phys. Rev. Lett.* **1996**, *77*, 3865.
- (50) Kresse, G.; Furthmüller, J. Efficient iterative schemes for ab initio total-energy calculations using a plane-wave basis set. *Phys. Rev. B: Condens. Matter Mater. Phys.* **1996**, *54*, 11169.
- (51) Kresse, G.; Joubert, D. From ultrasoft pseudopotentials to the projector augmented-wave method. *Phys. Rev. B: Condens. Matter Mater. Phys.* **1999**, *59*, 1758.
- (52) Blochl, P. E. Projector augmented-wave method. *Phys. Rev. B: Condens. Matter Mater. Phys.* **1994**, *50*, 17953.
- (53) Cazorla, C.; Stengel, M. Electrostatic engineering of strained ferroelectric perovskites from first principles. *Phys. Rev. B: Condens. Matter Mater. Phys.* **2015**, *92*, 214108.

(54) Cazorla, C.; Dieguez, O.; Iniguez, J. Multiple structural transitions driven by spin-phonon couplings in a perovskite oxide. *Sci. Adv.* **2017**, *3*, No. e1700288.